Journal of Wind Engineering & Industrial Aerodynamics 161 (2017) 17–26

Contents lists available at ScienceDirect

Journal of Wind Engineering and Industrial Aerodynamics

journal homepage: www.elsevier.com/locate/jweia

Assessing the potential of a commercial pulsed lidar for wind characterisation at a bridge site

Etienne Cheynet[a,*], Jasna Bogunović Jakobsen[a], Jonas Snæbjörnsson[a,b], Joachim Reuder[c], Valerie Kumer[c], Benny Svardal[d]

[a] Department of Mechanical and Structural Engineering and Materials Science, University of Stavanger, N-4036 Stavanger, Norway
[b] School of Science and Engineering, Reykjavik University, Menntavegur 1, 101 Reykjavik, Iceland
[c] Christian Michelsen Research AS, Fantoftveien 38, Bergen, Norway
[d] Geophysical Institute, University of Bergen, Allegaten 70, N-5007 Bergen, Norway

ARTICLE INFO

MSC:
00–01
99-00

Keywords:
Long-range pulsed lidar
Sonic anemometer
Long-span bridge
Length scale
Wind turbulence

ABSTRACT

Characterisation of atmospheric turbulence is a central step prior to the construction of long-span bridges. The present paper investigates the potential of a long-range scanning pulsed coherent lidar to measure the wind field at the inlet of a fjord. The wind velocity data acquired by the lidar is compared to the data recorded by sonic anemometers installed on the bridge. The focus is on the ability of the lidar to capture single and two-point statistics of turbulence in complex terrains. Satisfying results are obtained with the Line-of-Sight scanning mode, which provides the best sampling frequency (1 Hz). The low temporal resolution and the low signal-to-noise ratio for the Range Height Indicator and the Plan Position Indicator scanning modes are important limiting factors in the pilot study performed. Better results may be achieved for a lidar measurement set-up which is adapted specifically for investigating coherence.

1. Introduction

The construction of a long-span bridge in a complex terrain requires a detailed analysis of the local wind conditions. For wide and deep inlets, e.g. the fjords on the Norwegian West coast, this can be a challenging task that becomes even more difficult if no infrastructure can be used as support for wind sensors. Because of the large size of the spatial domain, a considerable number of anemometers would be required to provide a sufficient spatial resolution of the wind field in horizontal and vertical planes. In such conditions, the use of traditional wind sensors may become unfeasible.

The development of remote sensing technologies, especially in the field of long-range scanning pulsed coherent lidars, offers a possibility to acquire valuable data beyond the reach of traditional single-point wind sensors. Since around 2000, commercial wind lidars have been mostly used as wind-profilers for the need of atmospheric research (Reitebuch, 2012) or wind energy (Smith et al., 2006; Courtney and Wagner, 2008). A wind profiler measures the wind directly above the lidar and is therefore not adapted to monitor the flow along a bridge deck as it does not provide a better spatial resolution than an anemometer.

The recent development of wind lidars equipped with a rotating scanning head has extended their versatility. Contrary to a wind profiler, a scanning wind lidar can orientate the beam in any direction of the space or even be used as a wind profiler (Drew et al., 2013; Lane et al., 2013). Until now, comparisons between anemometers and scanning lidars for wind turbulence measurements have been limited to flat and homogeneous terrains. The distances between the anemometers and the lidars are most of the time less than 300 m, and only in some exceptional cases up to 800 m (Schneemann et al., 2014). Such comparisons can been conducted using three synchronized wind lidars (Mann et al., 2009), a dual-lidar system (Schneemann et al., 2014; Newsom et al., 2015) or a single lidar (Sjöholm et al., 2011). These studies consist often of direct comparisons between the measured time series and the corresponding mean wind velocities. In general a good agreement is observed, although the spectra measured by wind lidars is naturally low-pass filtered. This phenomenon, also called spatial averaging effect, results from the weighted average of the velocities located in a volume stretched along the scanning beam (Sjöholm et al., 2009, 2011). Although sonic anemometers also measure the flow in a volume, the latter is small enough with regard to the scale of turbulence studied so that sonic anemometers are considered as point-measurement devices.

The application of scanning wind lidars to measure atmospheric

* Corresponding author.
E-mail address: etienne.cheynet@uis.no (E. Cheynet).

http://dx.doi.org/10.1016/j.jweia.2016.12.002

Available online 05 January 2017

turbulence in complex terrains at distances beyond 1 km remains unexplored. This brings numerous uncertainties such as a larger measurement noise and an increased flow complexity. A comparison of the measured flow with reference data from sonic anemometers is therefore necessary. A review of lidar turbulence measurement done by Sathe and Mann (2013) shows that the turbulence intensity, the integral length scales or the wind coherence measured by Doppler lidars have been studied with only a limited focus on wind load estimation on structures spanning more than several hundred meters. New measurement configurations need therefore to be developed to adapt the lidar technology to bridge engineering applications.

In the present study, a long-range scanning pulsed coherent lidar was deployed at the inlet of a fjord between April and June 2014, as part of a joint research project between the University of Stavanger, the University of Bergen and Christian Mikkelsen Research. The purpose was to assess the ability of such a lidar to characterise atmospheric turbulence relevant to bridge engineering, i.e. the aforementioned mean wind velocity, turbulence intensity, turbulence length scales and wind coherence. This relies on a comparison between wind data measured by sonic anemometers located above the deck of a suspension bridge and those from a wind lidar located 1.75 km away, the scanning beam of which targets the bridge deck.

The present paper is organized as follows: first the bridge site and its instrumentation are presented. Then the lidar device is described as well as the different scanning configurations used. Results from the analysis relies on a comparison between the anemometers and lidar data in terms of statistics of wind turbulence. In addition, the influence of the topography on the flow homogeneity is investigated in details by the means of both lidar and anemometer data. Finally the potential and limits of future applications of a single or multiple wind lidars in the field of bridge engineering are discussed.

2. Measurement site and instrumentation

2.1. The lysefjord bridge site

The Lysefjord suspension bridge crosses the narrow inlet of the Lysefjord in Norway (Fig. 1). It has a main span of 446 m with an elevation of 55 m above the sea level at mid-span. It is oriented from North-West to South-East and is surrounded by steep hills with slopes ranging from 30° to 45° and a maximum altitude of 350 m to the North and 600 m to the South.

Two dominant wind directions are usually recorded by anemometers installed along the bridge span (Cheynet et al., 2016a). The flow from the inside of the fjord (N-NE direction) is more affected by the topography than the flow from the outside of the fjord (S-SW direction). In general the flow from N-NE is more turbulent whereas the flow from S-SW displays a larger wind velocity (Fig. 2). The S-SW flow may be influenced by a Venturi effect as it approaches the bridge, whereas the wind from N-NE may be disrupted by a small island located 1 km to the East side of the bridge with a maximum height of 54 m. This island is visible on the top-right panel of Fig. 1.

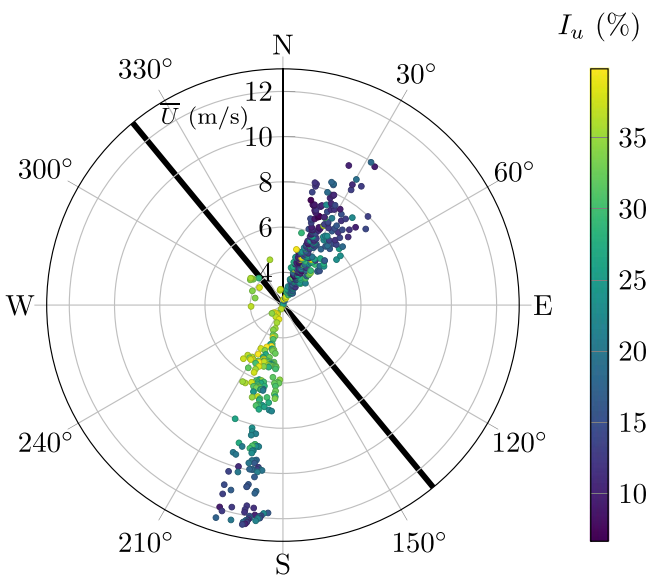

Fig. 2. 10 min averaged horizontal wind velocity, turbulence intensity and wind direction recorded by the anemometers on the bridge deck on 2014-05-22 (144 samples per sensor).

A number of studies conducted using wind profilers (Bingöl et al., 2009; Kim et al., 2016) suggest that biased estimates of the wind velocity may be obtained for mountainous terrains, with an error ranging from 2–10%. In the present study, this issue is avoided since the WINDCUBE 100S was not used as a wind profiler.

2.2. Sonic anemometers

Five sonic anemometers were installed on the Lysefjord Bridge on November 2013 (Fig. 3). Those located on hangers 16, 18, 20 and 24 are 3D WindMaster Pro sonic anemometers from Gill Instrument Ltd with a sampling frequency of 32 Hz. The one located on hanger 10 is a Vaisala weather transmitter WXT520, the sampling frequency of which is 4 Hz.

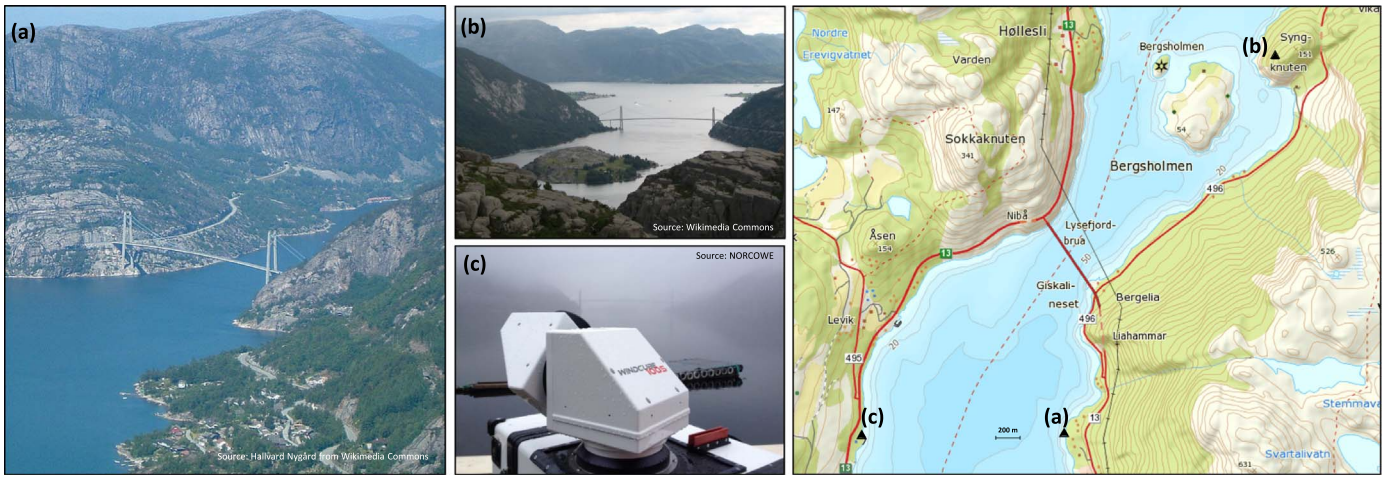

Fig. 1. Three different views from the bridge site: from the South-West (view (a), left), from the East (view (b), top centre), from the lidar location on the West (view (c), bottom centre), and their position on the map (right panel).

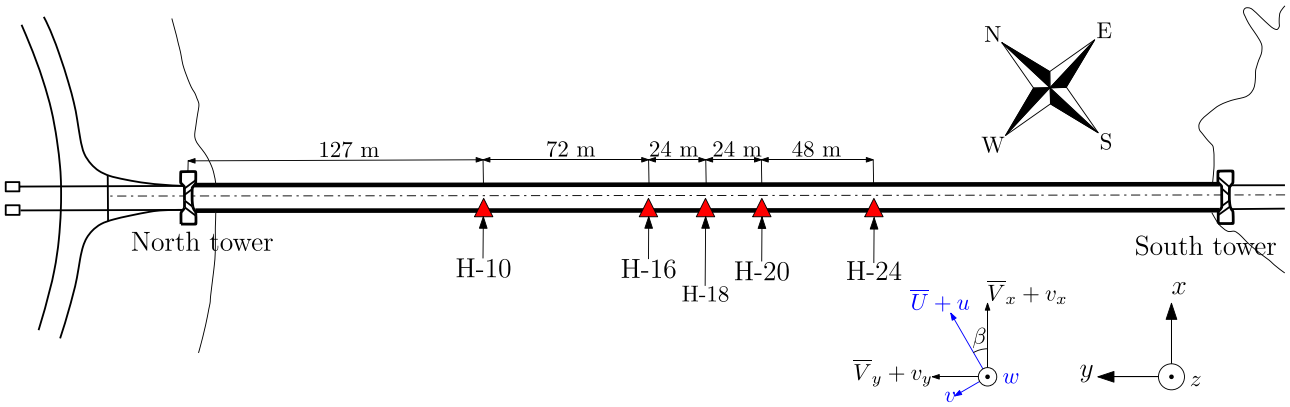

Fig. 3. Schematic of the anemometers installed near Hangers 10, 16, 18, 20, and 24, noted H-10, H-16, H-18, H-20 and H-24.

Fig. 4. Sonic anemometer fixed at a hanger (left) and at the top of a pole (right) at Lysefjord Bridge.

The anemometers are installed 6 m above the west side of the bridge deck and are either directly fixed to the hangers, or on the top of a vertical steel pole above the main cables (Fig. 4). The wind velocity components are continuously recorded at a sampling frequency of 100 Hz by several data acquisition units inside the bridge girder. The wind data are then synchronized, re-sampled at a sampling frequency of 20 Hz and transferred to a server via a mobile net.

The coordinate system for the wind components is defined in Fig. 3. The along-wind and across-wind components are denoted U and V respectively. The wind components normal and parallel to the deck span are denoted V_x and V_y respectively and are obtained by projection of the along-wind and across-wind components on the bridge axis. Each component is split into a mean component denoted by an overlined uppercase letter and a fluctuating component represented by a lower case letter (Eqs. (1)–(4)). Under stationary wind conditions, the across-wind component has a zero mean value (Teunissen, 1980).

$$U = \overline{U} + u \tag{1}$$

$$V = v \tag{2}$$

$$V_x = \overline{V}_x + v_x \tag{3}$$

$$V_y = \overline{V}_y + v_y \tag{4}$$

2.3. Doppler lidar

A pulsed Doppler wind lidar is required to monitor the flow at distances larger than 1 km. Continuous Wave (CW) wind lidar systems, such as the short-range WindScanner system (Mikkelsen et al., 2008) are not suitable for this purpose since the probe length averaging would be too large to provide useful data. A single long-range wind Doppler lidar was therefore deployed 1.75 km West of the Lysefjord Bridge, at an altitude of 5.7 m, between April and June 2014. The lidar is a WINDCUBE 100S from Leosphere and is characterized by a rotating scanning head allowing a higher versatility than the WINDCUBE V1 from which it is inspired. Three different scanning modes were used: PPI (Plan Position Indicator), RHI (Range Height Indicator), and LOS (sequential fixed Line-Of-Sight measurement). The Velocity-Azimuth Display (VAD) mode was not used here as the flow above the lidar is likely to be different from the flow at the bridge site. In addition, Sathe et al. (2011) observed that the VAD technique was not appropriate to fully capture the wind turbulence, and a six-beam configuration may have to be used instead (Sathe et al., 2015).

The WINDCUBE 100S measures simultaneously the wind velocity at several positions along the scanning beam. Given an azimuth angle Φ, an elevation angle θ and a radial distance r, the lidar is designed to measure the along-beam wind velocity component (Fig. 5). In the present paper, the azimuth angle is defined with respect to North, and the elevation angle is defined with respect to the horizontal plane. The PPI, RHI and LOS scanning modes can be defined by using only the azimuth and the elevation angle. The PPI scan is run for a fixed elevation and multiple azimuth angles, whereas the RHI scan is run for a fixed azimuth but multiple elevations angles. The LOS scan is run for a fixed azimuth and a fixed elevation angle. The PPI scan used here is actually a “PPI sector scan” as the scanning beam does not describe a full circle. For the sake of brievety, the “PPI sector scan” is simply referred to as the “PPI scan” in the following. The definition of these scanning modes is identical to the one used with Doppler radars which have been applied in the field of wind energy (Hirth et al., 2008). No Doppler wind radar was utilized in the present study, although the one used by e.g. Hirth et al. (2008) presents multiple advantages for bridge engineering, in particular a larger maximum range or a higher scanning speed than the lidar we used.

Some early works using RHI and PPI scans with wind lidars have

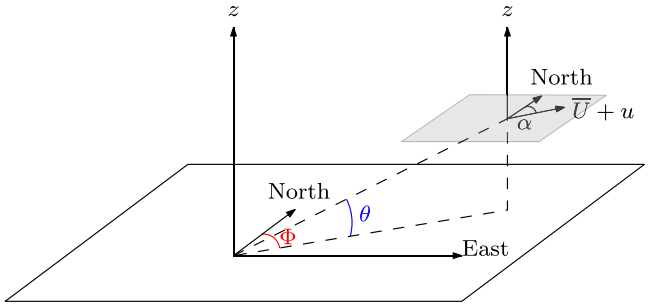

Fig. 5. Coordinate system of the WINDCUBE 100S.

been carried out e.g. by Grund et al. (2001) for atmospheric research, or by Banta et al. (2004) in complex terrains, with a focus on the influence of the topography on the wind field. To the authors' knowledge, none of these scanning modes have previously been used with a single lidar to study details of atmospheric turbulence for applications in bridge engineering.

The Carrier-to-Noise Ratio (CNR) is defined as the Signal-to-Noise Ratio (SNR) on the carrier frequency. The minimum threshold value for the CNR is fixed to −27 dB, as by Kumer et al. (2014). If the threshold of −23 dB advised by Pearson et al. (2009) is used in the present study, the availability of the data is drastically reduced. Moreover, time series recorded with a CNR between −23 dB and −27 dB showed an acceptable agreement with the anemometer data.

2.3.1. Case of a S-SW wind

For a wind from S-SW, a LOS scan was carried out on 2014-05-22 from 16:12:06 to 16:20:00 and time series made of a succession of 475 snapshots were created along the beam. The PPI and RHI scans were run later, from 16:50:22 to 17:25:44 and from 16:51:06 to 17:26:31 respectively. These scans were alternated so that time series made of 28 snapshots were produced. The key parameters of the scanning patterns for a S-SW wind are summarized in Table 1.

The PPI scan was used for three different elevation angles and the one at 1.8° was chosen so that the laser beam crosses the bridge deck. For the PPI scans conducted with an elevation of 0.8° and 1.8°, the accumulation time was 0.2 s with a scanning speed of 5°. For the elevation of 3.2°, the accumulation time was increased to 0.4 s with a scanning speed reduced to 2.5°. For these elevation angles, the lateral spatial resolution is 31 m at the position of the bridge deck, which corresponds to an azimuth increment of 1°. The RHI scan was conducted for three different azimuth angles with an accumulation time of 1 s and an elevation increment of 1°, which leads to a vertical resolution of 31 m at the position of the bridge deck. In the present paper, the study of the LOS scan is done by analysing time series obtained 1.71 km far away from the lidar, for an elevation angle of 1.8° and an azimuth angle of 38°, so that the beam aims at the middle of the bridge deck. For this scanning mode, the sampling frequency is 1 Hz. The lidar was setup with 256 equidistant overlapping range gates of 25 m length over the maximum range of 2500 m. The splitting of the maximum range of 2500 m into 256 equidistant range gates results in an along-beam resolution of about 10 m.

2.3.2. Case of a N-NE wind

When the flow comes from the inside of the fjord, the CNR is usually low and the number of lidar records for winds from N-NE is therefore limited. A low CNR may be explained by a higher turbulence intensity, an increasing complexity of the topography and the longer distance to the lidar.

A succession of 27 PPI scans could still be carried out on 2014-05-22 between 09:30:03 and 10:13:16 for a N-NE wind situation. The accumulation time was increased to 1 s, with a spatial resolution of 9 m along the bridge deck, and a range for the azimuth angle sector reduced to 30–46°. The sampling time was 136 s, which unfortunately did not allow a detailed time series analysis. The higher accumulation time and the lower velocity of the rotating head increased however the CNR, which allowed an analysis of the mean wind field at longer distance from the lidar.

Table 1
Parameters used for each scanning scenario (S-SW wind).

Parameters	PPI	PPI	RHI	LOS
Azimuth (°)	13 to 63	13 to 63	37, 38 and 39	25
Elevation (°)	3.2	0.8 and 1.8	0 to 6	1.8
Sampling frequency (Hz)	0.0128	0.0128	0.0128	1
Scan speed (°/s)	2.5	5	1	–
Accumulation time (s)	0.4	0.2	1	1
Approximate duration (min)	35	35	35	8

2.4. Along-beam wind velocity

The comparison between the lidar and the anemometers is relevant only if the wind data are analysed in the same coordinate system. Since the scanning lidar measures the line-of-sight wind velocity only, the wind records from the anemometers must be transformed into a spherical coordinate system (Lhermitte, 1969):

$$V_r = \sqrt{U^2 + V^2}\cos(\alpha - \Phi)\cos(\theta) + W\sin(\theta) \tag{5}$$

where α is the wind direction recorded by the anemometers. The along-beam wind velocity can be expressed in the bridge-based coordinate system using:

$$V_r = V_x\sin(\Phi + \gamma)\cos(\theta) - V_y\cos(\Phi + \gamma)\cos(\theta) + W\sin(\theta) \tag{6}$$

where γ is the bridge orientation from the North, equal to 39.5°. The along-beam wind component becomes therefore equal to V_x if the azimuth angle is equal to 50.5°.

2.5. Turbulence length scales

The line-of-sight wind velocity V_r. is split into a mean and a fluctuating part denoted $\overline{V_r}$ and v_r. respectively. Using this definition, a modified turbulence length scale is introduced to capture the extent of the wind gusts propagating along the scanning beam. The integral length scale $L^x_{v_r}$ is calculated by assuming that Taylor's hypothesis of frozen turbulence applies for the along-beam wind velocity:

$$L^x_{v_r} = \overline{V_r}\cdot\int_{t=0}^{t(R_\tau(t)=0)} R_\tau(t)\,\mathrm{d}t \tag{7}$$

where R_τ is the single-sided auto-covariance function of the fluctuating along-beam wind velocity calculated with a time lag τ. More specifically, the integral time scales are calculated by integrating the auto-covariance function from a zero time lag up to the time lag corresponding to the first zero-crossing of the auto-covariance (Lenschow and Boba Stankov, 1986).

The turbulence length scale $L^y_{v_r}$ along a horizontal line normal to the scanning beam is computed with the PPI sector scan for a set of different azimuth angles and a single distance to the lidar using:

$$L^y_{v_r} = \int_0^{+\infty} R_{v_r v_r}(\eta)\,\mathrm{d}\eta \tag{8}$$

where $R_{v_r v_r}$ is the vector containing the correlation coefficients of the along-beam wind velocity, calculated at two separated spatial points along the arc created by the scanning beam. For small angles and a large distance from the lidar, this arc can be approximated by a line segment.

2.6. Wind spectra

The power spectral density (PSD) of the along-beam velocity component is calculated using the lidar measurements from the LOS scan, and compared to the one calculated from the sonic anemometer records. The PSD are computed using Welch's overlapped segment averaging estimator (Welch, 1967), based on two segments and 50% overlapping. The PSD is afterwards bin-averaged using a logarithmically spaced interval to reduce the high-frequency noise. The wind spectra are expressed as a function of the modified wavenumber k, which is based on the hypothesis of Taylor's frozen turbulence, and is here defined as:

$$k = \frac{2\pi f}{\overline{V_r}} \tag{9}$$

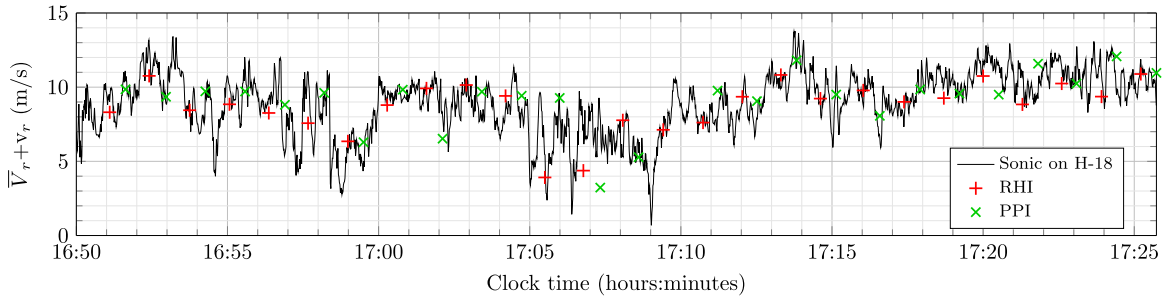

Fig. 6. Along-beam wind velocity from the PPI scan, the RHI scan and the anemometer on H-18 on 2014-05-22 (S-SW wind).

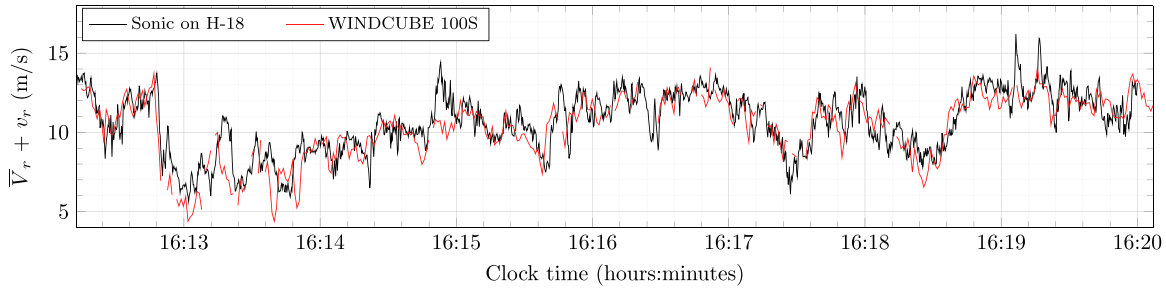

Fig. 7. Along-beam wind velocity from the LOS scan and the anemometer on H-18 on 2014-05-22 (S-SW wind).

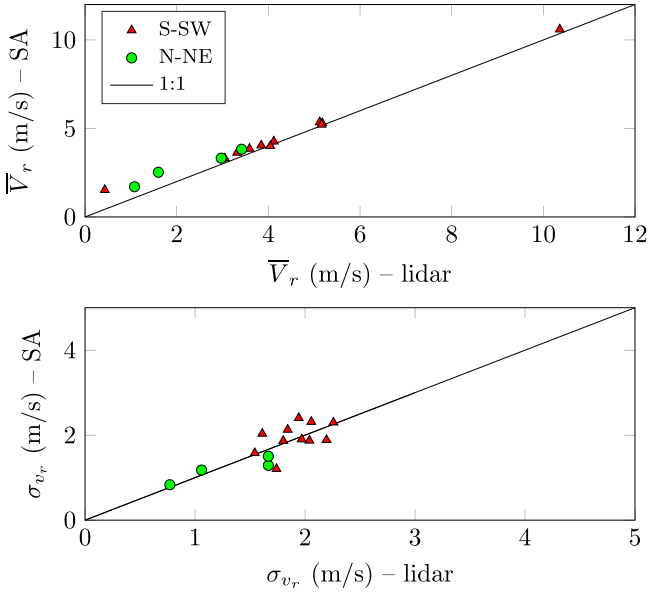

Fig. 8. Mean value and standard deviation of the line-of-sight wind component measured by the lidar and the sonic anemometer (SA) on H-18. The data set used is recorded on 2014-05-22 between 10:56 and 16:20 with the LOS scanning mode (15 samples of 8–10 min duration).

3. Results and discussions

3.1. Single-point statistics of wind turbulence

In a first step, the times-series obtained from the lidar records are directly compared to those from the anemometers (Figs. 6–7). If the CNR of the wind records at the bridge deck position is too low, then the time series are recorded in a volume located 40 m upstream of the bridge instead. In that case, Taylor's hypothesis of frozen turbulence is assumed valid and is used to correct the time shift introduced by the spatial gap. For an along-beam wind velocity $\overline{V}_r = 10$ ms^{-1} for example, the time lag is set to 4 s for the PPI scan. This correction has been done for the PPI and RHI scans, as well as the LOS scan carried out from 16:12 to 16:20 on 2014-05-22. An estimation of the time lag by using the cross-correlation between the lidar and anemometer signals could not be carried out because of the insufficient correlation between the two signals.

According to e.g. IEC (2005), the mean wind velocity should be calculated over a 10 min period. In the present paper, the mean wind velocity is based on the length of the available data, ranging from ca. 8 min (for the LOS scan) to ca. 35 min (for the PPI and RHI scans). For the PPI and RHI scans, a detailed comparison with a single anemometer may not be statistically meaningful, because of the low sampling frequency used, even if a satisfactory agreement may be expected according to Fig. 6. The low CNR is an additional limiting factor which prevents a detailed analysis of the single-point statistics of atmospheric turbulence for the PPI and RHI scans.

The LOS scan may overcome these issues, even if some abrupt variations of the wind field recorded by the anemometer are not captured by the lidar. On Fig. 7, the along-beam velocity from the LOS scan is measured for an elevation angle of 1.8°, an azimuth angle of 38°and at a distance of 40 m upstream to the bridge deck. It is compared to the anemometer data after correction of the time lag following the method presented above. Results suggest that this simple correction is good enough as a first approximation. The lidar and anemometer data displayed in Fig. 7 show a difference of only 2.1% for the mean along-beam wind velocity and 3.6% for its standard deviation.

A more detailed analysis of the LOS scanning mode is made by including multiple 10 min samples obtained on 2014-05-22 between 10:56 and 16:20 (Fig. 8). Even at low wind velocity, i.e. lower than 5 ms^{-1}, a good agreement is obtained between the lidar data and the anemometer measurements, although a slightly larger dispersion is observed for the standard deviation of the along-beam component. This is in agreement with the results of Mann et al. (2009) who observed only a marginal effect on the data quality for low wind velocities, even though the CNR decreases. An additional source of discrepancy may also be explained by the fact that anemometers provide more or less single-point measurements whereas Doppler wind lidar are monitoring the wind field in a volume.

The azimuth increment for the PPI scan is small enough to study the correlation or the homogeneity of the wind velocity along the bridge span. For the RHI scan and the bridge in question, the vertical spatial resolution is too low to analyse the wind field close to the deck. As our

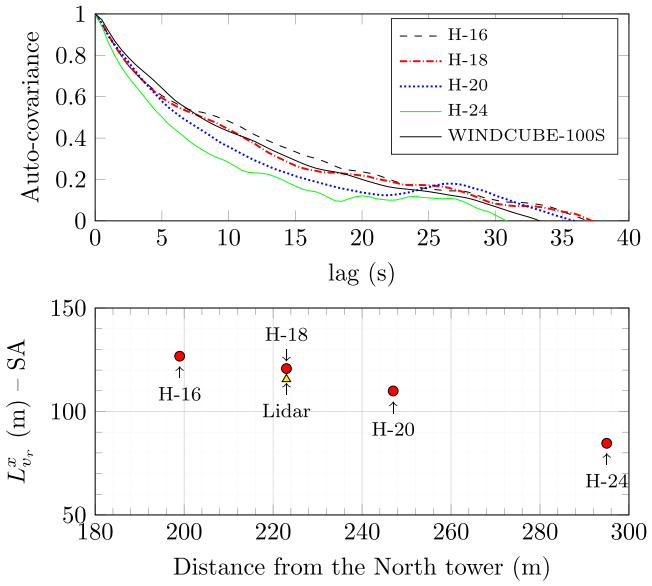

Fig. 9. Top: auto-covariance function for the LOS scan and the corresponding anemometer records, with $\overline{V}_r = 10.4\ \mathrm{ms}^{-1}$. Bottom: along-beam integral length scales from the sonic anemometers on H-16 to H-24. The data set used is recorded on 2014-05-22 between 16:12 and 16:20 (Fig. 7).

investigations indicate certain limitations of the RHI scan pattern for a turbulence investigation at a suspension bridge, we consequently have not included that data set in the following discussion.

The modified integral length scale $L^x_{v_r}$ is calculated using Eq. (7) and displayed for each sensor with the underlying auto-covariance functions in Fig. 9. The auto-covariance functions are calculated using detrended wind records to reduce the influence of any non-stationarity fluctuations on the integral length scale. The re-sampling process carried out for every anemometer had no visible consequences on the estimation of the integral length scale. The value found on Fig. 9 by the lidar for $L^x_{v_r}$ is compatible with the values found by the anemometers on H-16, H-18 and H-20. The measured integral length scales tend to increase towards the North tower (bottom panel of Fig. 13). The along-span fluctuations of $L^x_{v_r}$ are not due to the varying azimuth angle. A similar increase of the along-wind integral length scales toward the North tower is indeed recorded by the sonic anemometers. Based on wind tunnel tests, Hui et al. (2009) have observed remarkable variations of the integral length scale along the Stonecutter Bridge for an over-land exposure. This suggests that non-uniform flow may be more common than expected for complex topographies.

In Fig. 10, a more general comparison of the along-beam integral length scale shows a good overall agreement between the lidar data and the anemometer measurements. Among the 15 samples used, only one outlier was observed, which was probably due to some non-stationary fluctuations that could not be corrected by simply removing the linear mean trend from the wind data.

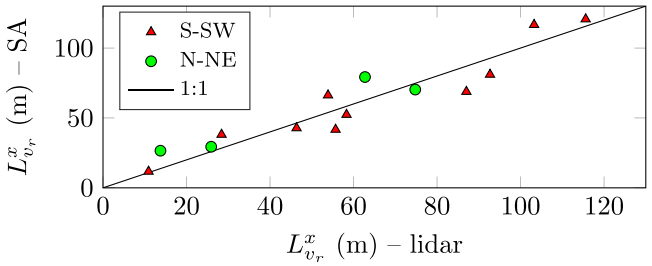

Fig. 10. Integral length-scales for the line-of-sight component, based on 15 samples recorded on 2014-05-22 between 10:56 and 16:20 by the lidar and the anemometer on H-18 (1 outlier removed).

3.2. Spectral analysis

The wind spectra is studied first for the along-beam velocity recorded from 16:12:06 to 16:20:00 on 2014-05-22, then for 7 of the 15 sample studied on 2014-05-22 between 10:56 and 16:20 (Fig. 11). The selection of a reduced number of samples is justified by the need to use a stationary wind direction. If the wind direction shows a large variability, the lidar spectra may have little meaning as the spatial averaging effect is affected by the angle between the beam and the wind direction.

On the top panel of Fig. 11, a good overall agreement is observed between the PSD calculated from the anemometers and the lidar data. By comparing the wind spectra measured with a modified WINDCUBE and a sonic anemometer, Sjöholm et al. (2011) observed that the spatial averaging effect was clearly visible for wavenumbers larger than $0.06\ \mathrm{m}^{-1}$. In the bottom panel of Fig. 11, the spatial averaging effect becomes clear for wavenumbers above 0.1^{-1} and is not clearly visible in the top panel. This indicates that the lidar data contains measurement noise which may be due to the relatively low threshold value for the CNR and the larger scanning distance.

The value of the angle between the wind direction and the beam orientation may also play a non-negligible role on the spatial averaging effect (Sjöholm et al., 2011). In the present study, this angle was fluctuating between 10°and 20°. The evolution of the spectral transfer function with the angle between the wind direction and the beam orientation will be investigated in a further study.

3.3. Two-point statistics of wind turbulence

The cross-correlation coefficients for volumes measured along a line parallel to the deck are calculated 40 m upstream of the bridge, by using the wind data from the PPI scan obtained on 2014-05-22 between 16:50:22 and 17:25:44. During that period, the averaged mean along-beam wind velocity measured by the lidar was $\overline{V}_r = 8.6\ ms^{-1}$. Eight azimuth angles ranging from 36°to 43°, i.e. for positions along the bridge located between H-09 to H-24, are used. The range of the azimuth angles is assumed small enough so that the arc created by the scanning beam can be approximated by a line segment. The angle between this line segment and the bridge deck is ca. 11.5°, which is considered small enough so that the non-parallelism has little consequences on the comparison between the lidar and the anemometers. The anemometers installed from H-16 to H-24 are used to calculate the reference correlation coefficients that are compared to those measured by the lidar in Fig. 12.

The correlation coefficients for the lidar data show a satisfactory agreement with the results provided by the anemometers, despite the low sampling frequency of the lidar and the low CNR of the signal, which may explain the considerable scatter. The corresponding modified turbulence length scales $L^y_{v_r}$ for the PPI scan and the anemometer data are 163 m and 193 m respectively. It should be noted that these length scales are not appropriate for the estimation of buffeting loads. Firstly because they are calculated based on the line-of-sight wind component, and secondly because the sampling interval does not allow a detailed investigation of the co-coherence. The Nyquist frequency for the present PPI scan is 6 mHz, which is too low for a corresponding co-coherence analysis.

3.4. Requirement for coherence analysis

The results from the analysis of the PPI scan recorded at Lysefjord, and the co-coherence calculated from the anemometer data suggests that lidars may have the potential to give useful estimates of the co-coherence under certain conditions. For the along-wind component and for lateral separations above 30 m, the instantaneous rate of change of the co-coherence is usually low for frequencies larger than 0.10 Hz. Consequently, a sampling frequency between 0.20 Hz and

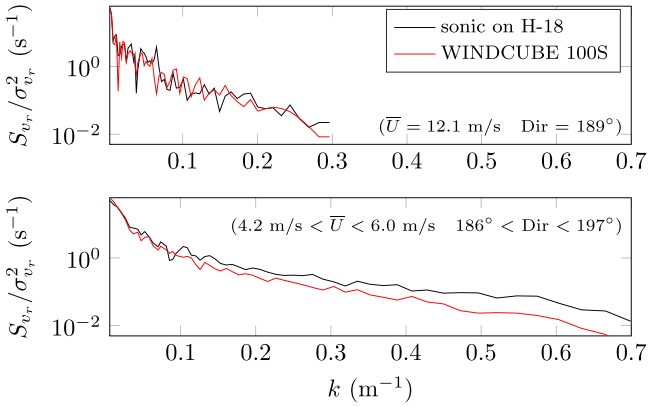

Fig. 11. Top: PSD of the recorded time series between 16:12:06 and 16:20:00. Bottom: PSD averaged over 7 samples recorded between 12:10 and 13:20 on 2014-05-22.

0.25 Hz should be sufficient to accurately fit the co-coherence using an exponential decay function like the one used e.g. by Davenport (1961) or Jakobsen (1997).

Let us consider a lidar aiming at a point 2 km away and using an accumulation time large enough to provide a satisfactory CNR, i.e. 0.4–0.5 s. The lateral distance is limited to 150 m with a spatial resolution of 30 m. Under these conditions, the arc created by the lidar can be approximated by a line segment. The horizontal wind velocity component normal to that line is denoted V_x. This configuration provides a sampling frequency of 0.20–0.25 Hz at the extremities of the scanned area, i.e. 0.40–0.50 Hz at its centre. The sweeping angle, i.e. the difference between the initial and final azimuth angles, would be lower than 5°, which is small enough so that the along-beam component V_r. can be assumed equal to V_x. To optimize data availability and to study the two-point statistics of atmospheric turbulence with a sufficient time and spatial resolution, a single elevation angle is required. To reach an altitude of 60 m at a distance of 2 km from the scanning lidar, an elevation angle of 1.7° is sufficient and small enough so that the influence of the vertical flow on the along-beam wind component can be neglected. At the end of 2015, such a scanning configuration was investigated in offshore environment with encouraging preliminary results (Cheynet et al., 2016b).

3.5. Homogeneity of the wind field

3.5.1. Case of a S-SW wind

During the measurement period ranging from 16:50:22 to 17:25:44 on 2014-05-22, the wind direction was assumed stable enough to derive representative averages of the along-beam wind velocity over the different snapshots. The measured PPI scans give the opportunity to investigate the horizontal homogeneity of the wind field in more detail. Fig. 13 presents the corresponding PPI scan for an elevation of 3.2° for a S-SW wind inflow case. A close-up for the nearest 300 m to the bridge is shown in Fig. 14. The azimuth of 0°corresponds to the North

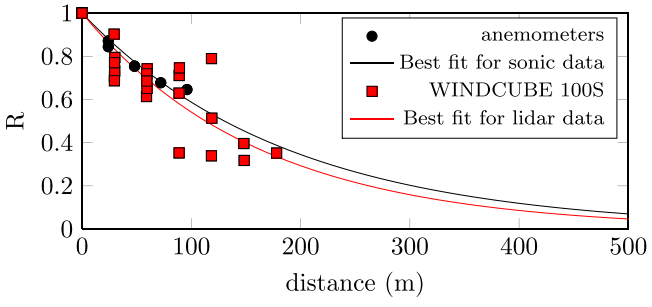

Fig. 12. Along-span correlation coefficients measured with the PPI scan of the lidar (squares) and the anemometers (circles) for the S-SW wind case on 2014-05-22.

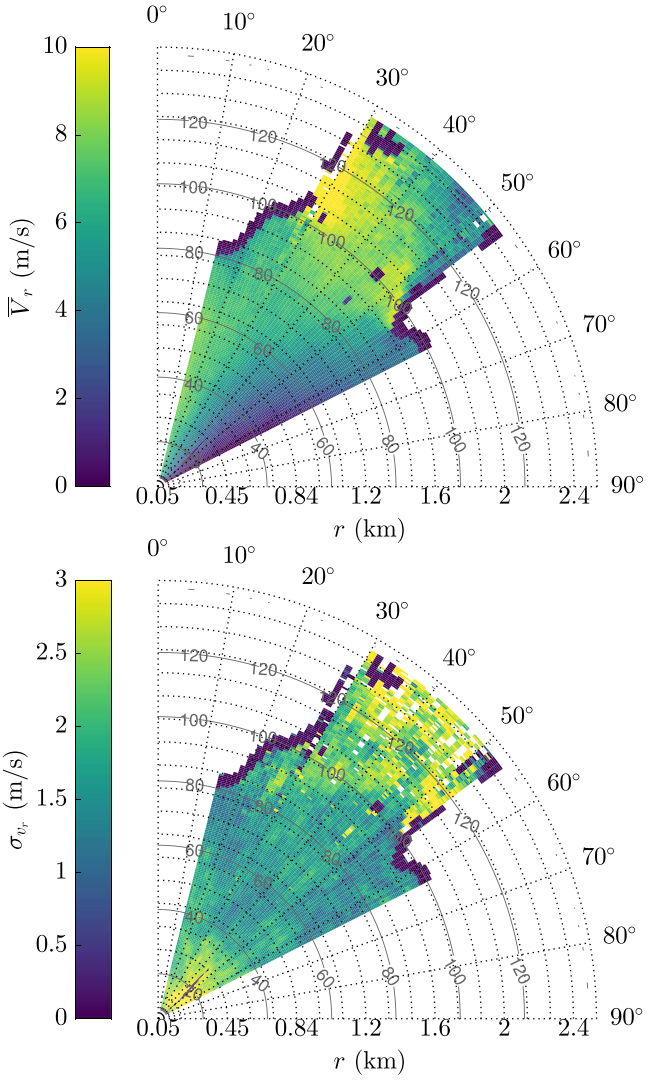

Fig. 13. Mean (top) and standard deviation (bottom) of the along-beam wind velocity derived from PPI scans recorded on 2014-05-22 between 16:50:22 and 17:25:44 with an elevation of 3.2°. The wind was blowing from S-SW with $\overline{V}_x$ = 8.0 ms^{-1} at the bridge site. The radial grey contour indicates the altitude (in meters) above the sea level.

direction whereas the azimuth of 90°corresponds to the East direction. In the S-SW wind, the lidar measures positive velocities since the particles that backscatter the emitted light move away from the lidar.

On Fig. 13, the towers are clearly visible as dark spots with a wind velocity close to 0 ms^{-1}, giving a clear contrast to the surrounding flow. The South tower is visible for an azimuth angle of 46° and a distance of 1.7 km from the lidar. It is slightly more difficult to detect the North tower which is visible for an azimuth angle of 32°and a distance of 1.8 km from the lidar. The range of the observable data is limited by dark borders. The latter indicate wind speed and standard deviation of 0 ms^{-1} and are due to the effect of the mountainous terrain on the measured flow. The mean wind velocity $\overline{V}_r$ increases when the flow joins the corridor crossed by the bridge and is higher near the North tower, downstream of the bridge. It is unsure whether the wake created by the towers is visible or not as the maximal height of the towers is 102 m whereas the beam is scanning at a slightly higher altitude beyond the bridge position. Near the South tower, a strong gradient of the radial wind velocity is apparent, potentially indicating turbulent flow separation. Additional lidar records may be required to confirm these observations.

An apparent inhomogeneity on Fig. 13 may result from the dependency of the along-beam wind velocity on the azimuth angle. Therefore, the homogeneity of the wind field cannot be properly

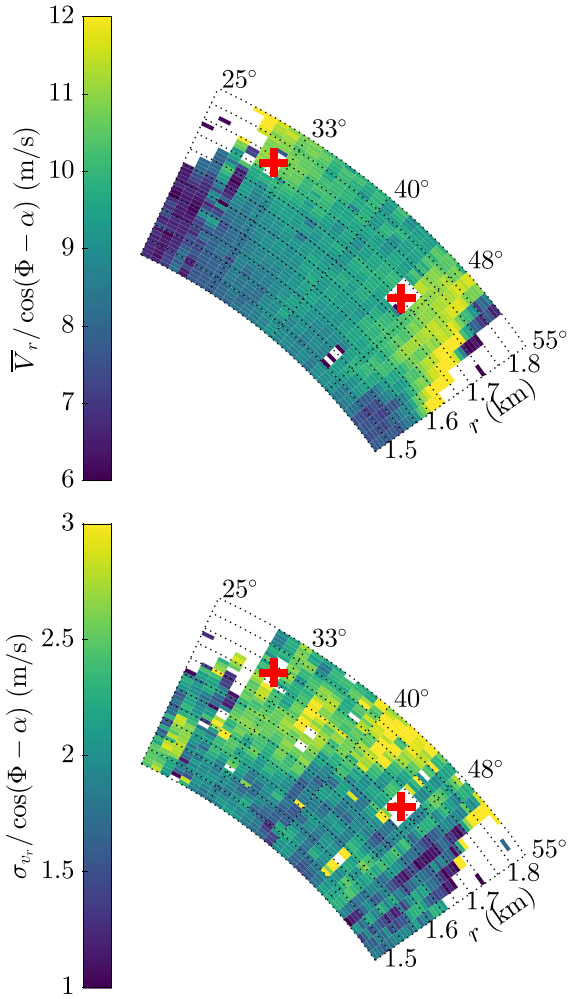

Fig. 14. Close-up of the PPI scan with the mean (top) and standard deviation (bottom) of the corrected along-beam wind velocity on 2014-05-22 between 16:50:22 and 17:25:44. The towers are shown as thick crosses.

discussed if the PPI scan is based on the along-beam wind velocity alone. For small elevation angles, the horizontal mean wind velocity component can be retrieved according to Eq. (5) by dividing the mean radial wind velocity by $\cos(\alpha - \Phi)$, where α is the wind direction and Φ is the azimuth angle. In the present analysis, this operation is only relevant near the bridge deck, where the mean wind direction is known from the sonic anemometer measurements. For wider azimuth angles and a larger distance to the bridge, the uncertainties related to the mean wind direction increase. The correction was therefore applied for the case of the close-up of the bridge deck only, on Fig. 14, where the mean wind direction α is assumed uniform and equal to 190°.

On Fig. 15 the mean and standard deviation of the wind velocity component $\overline{V}_x$ and the wind direction measured by the anemometers are almost uniform near the bridge centre, but increase toward the North tower. On the bottom panel of Fig. 14, the standard deviation of the radial wind velocity σ_{v_r} seems also to increase towards the North tower. However, the largest fluctuations for the standard deviation appear to occur on the South part of the bridge deck.

On the bottom panel of Fig. 13, it can be seen that the standard deviation of the radial wind velocity downstream of the bridge, i.e. for radial distances greater than 1.8 km, shows a less reliable data structure than for the upstream flow. This loss of information is most likely related to the increased distance and low CNR recorded but may also be influenced by greater turbulence in the downstream flow. The associated inaccuracy prevents any deeper data analysis of the wind field downstream of the bridge deck.

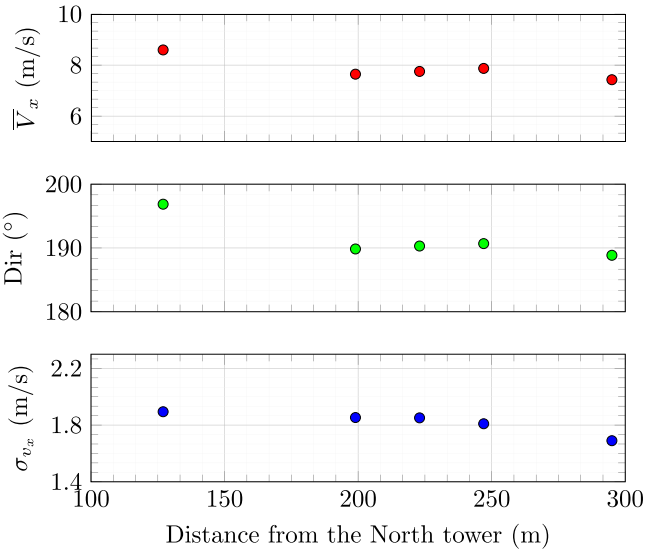

Fig. 15. Mean wind velocity (top), mean wind direction (middle) and RMS of the wind velocity (bottom) along the bridge, based on anemometer records between 16:50:22 and 17:25:44 on 2014-05-22.

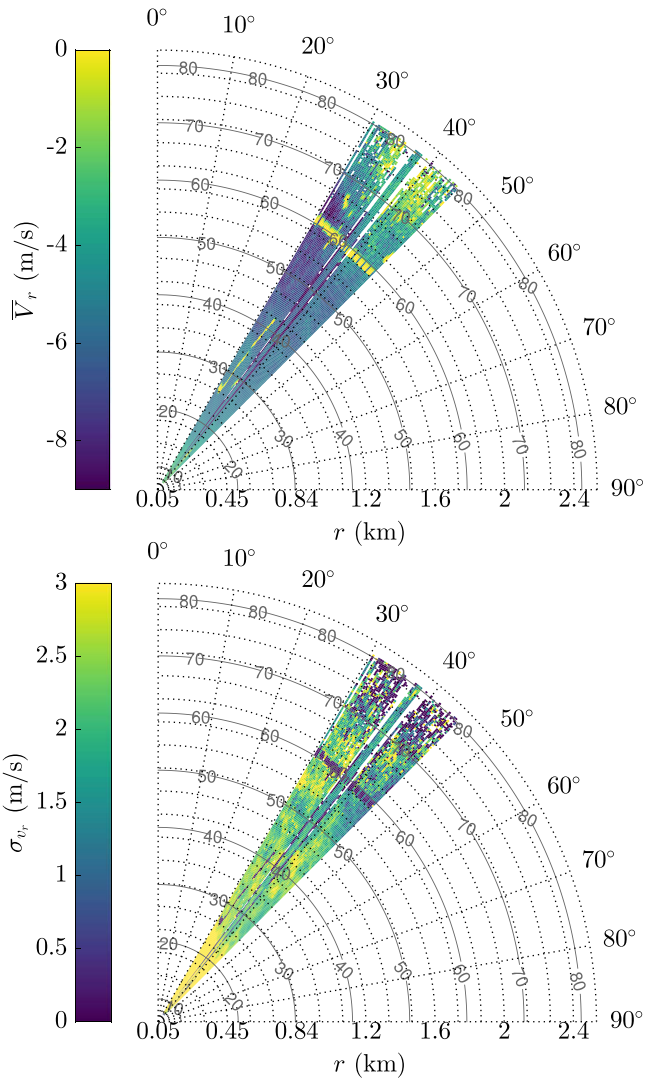

Fig. 16. Mean (top) and standard deviation (bottom) of the radial wind velocity derived from the PPI scan recorded on 2014-05-22 between 09:30:03 and 10:13:16, with an elevation of 1.8°. The wind was blowing from N-NE with $\overline{V}_x = 6.0\ \mathrm{ms}^{-1}$ at the bridge centre. The radial grey contours indicate the altitude (in meters) above the sea level.

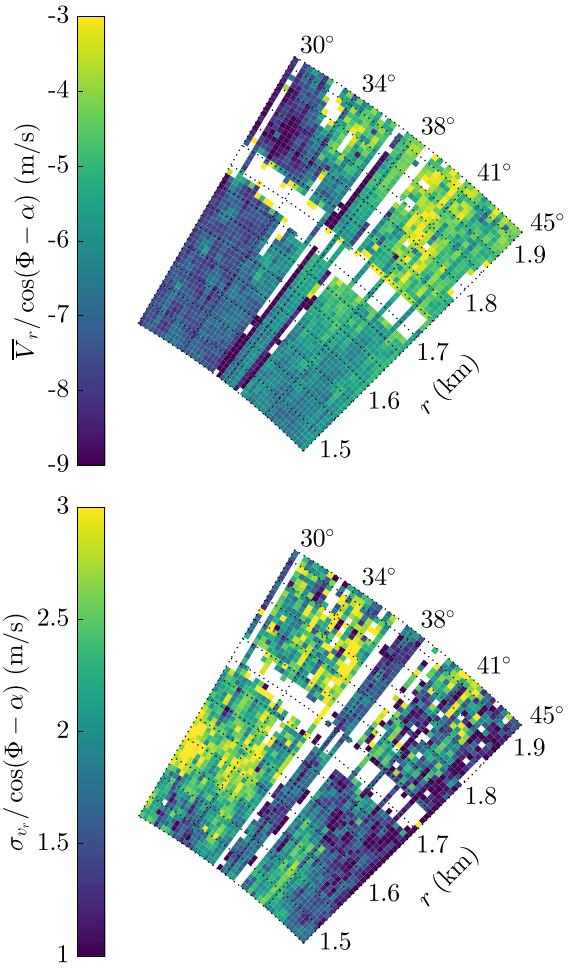

Fig. 17. Close-up of the PPI scan with the mean (top) and standard deviation (bottom) of the corrected radial wind velocity on 2014-05-22 between 09:30:03 and 10:13:16. The deck is visible as a white strip for r=1.7 km.

3.5.2. Case of a N-NE wind

For the N-NE wind situation, Figs. 16–17 show that the flow from N-NE is more heterogeneous near the bridge than for a S-SW wind. The North side of the deck displays a higher wind velocity than the South part, indicating a wake effect of the bridge structure. A closer view to the bridge in Fig. 17 shows that the non-homogeneity of the flow downstream to the deck is more complex than expected. Because the North side of the deck is higher than the south side, the lidar detects the wake for a limited portion of the bridge only. Consequently, a locally higher turbulence intensity may be recorded where the scanning beam crosses the wake created by the deck. Another source of non-uniformity may be the island located 1 km to the East side of the deck, the wake of which may be visible in Fig. 16.

The close-up of the flow near the bridge deck on Fig. 17 is corrected in a similar fashion as in Fig. 14, with a mean wind direction α assumed uniform and equal to 30°. Because the scanning head of the lidar sweeps a narrower area for the N-NE wind, the correction is less effective for that wind direction. The anemometer measurements presented in Fig. 18 confirm that the mean and standard deviation of the wind velocity are much higher near H-10 with values about 7.0 ms^{-1} and 2.2 ms^{-1} respectively. The evolution of the wind direction along the span has however the same order of magnitude as the S-SW wind situation studied previously. The North side of the deck shows stronger wind fluctuations than the South part which is likely a consequence of the non-uniformity of the mean wind velocity along the span.

The relatively good spatial resolution of the PPI scan shows its potential to study the effect of topography on the flow uniformity along a bridge deck. This can be particularly useful for longer spans and wider fjords, but such conditions require a lidar with a longer range than the one used in the present study.

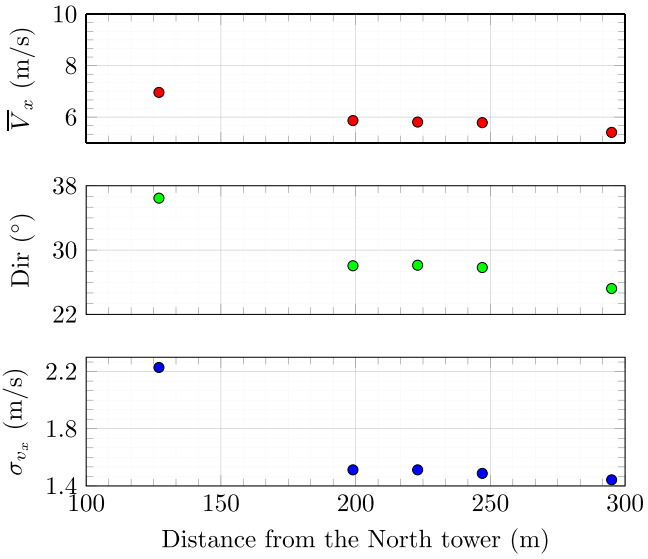

Fig. 18. Mean wind velocity (top), mean wind direction (middle) and RMS of the wind velocity (bottom) along the bridge, based on anemometer records between 09:30:00 and 10:10:00 on 2014-05-22.

3.6. Toward a multi-lidar configuration

A complete description of the flow upstream of a suspension bridge requires measurements of both the horizontal and vertical wind components. For a relatively flat terrain, measurements of the wind components normal to a bridge deck could be conducted first by using a single lidar as proposed in Section 3.4. Then, measurements of the vertical wind component could be done by using the method applied by Lothon et al. (2006), Lothon et al. (2009) which is based on a LOS scan with an elevation angle of 90°.

Simultaneous measurements of different wind components is not achievable if only a single wind lidar is used. Dual or tri-lidar configurations may overcome this challenge. To monitor the flow upstream of a future long-span or super long-span suspension bridge, the multi-lidar system needs to be based on long-range pulsed lidars. The limited range of CW lidars restrains their application despite their encouraging performances to measure 2-D flows at a smaller scale (Sjöholm et al., 2014; Lange et al., 2015; Simley et al., 2016).

If a system of dual wind lidar is available, the method proposed by Newsom et al. (2015) to retrieve the three wind components may be considered. However, this configuration may not be compatible with the need to use a sampling frequency of at least 0.2 Hz to properly measure wind coherence. This constraint may be overcome by using a system of three synchronized lidars. Encouraging results have been obtained at an experimental site by e.g. Mann et al. (2009) or Fuertes et al. (2014) with the tri-lidar technology. Such results have yet to be validated in a real-case situation, i.e. where the flow is measured several kilometres from the scanning devices.

4. Conclusion

A long-range scanning pulsed coherent lidar was installed 1.75 km West of the Lysefjord Bridge to analyse the wind field in the vicinity of the deck. Different scanning modes were used to study the single and two-point statistics of wind turbulence as well as the flow homogeneity. The data evaluated based on the lidar observations were compared to the wind records from anemometers installed along the bridge deck.

The uniqueness of this study is emphasized by the complex topography surrounding the measurement devices, where high mountains, steep hills and sea-land transitions are likely to influence the flow. The distance at which the lidar has measured the flow is considerably larger than in most previous studies, which constituted a new challenge for the device used.

The LOS scan and the anemometer data showed a satisfying agreement for the mean value and standard deviation of the line-of-sight wind velocity. In addition, the LOS scan provided a good estimation of the single-point wind spectrum, although a deeper investigation is required to better evaluate the spatial averaging effect. The compatibility between the anemometer and lidar data for the description of the wind field uniformity along the bridge span suggests that lidars may complement anemometers to study the wind effects on large wind-sensitive structures.

The PPI scan may be used to measure the coherence along the bridge span thanks to the good spatial resolution it provides. In the present study, the sampling frequency was too low to calculate the co-coherence, which is a fundamental parameter in estimating the dynamic wind load. The low CNR and the low sampling frequency are at present two technical limitations that reduce the applicability of long-range Doppler wind lidars for wind coherence measurement. An additional issue is the nature of the along-beam wind velocity, which depends by definition on the lidar position and the wind direction. The latter issue may be partially overcome for long-span suspension bridges by using small sweeping angles and a large scanning distance.

Future applications of lidars for a more complete characterisation of turbulence for bridge engineering purpose will rest on further improvements of lidar measurement capabilities as well as the use of two or three synchronized measurement units. Lidars clearly have the potential to play a prominent role in complementing traditional anemometers for monitoring the wind conditions in the vicinity of future long-span bridge sites.

Acknowledgements

The measurements were performed with the support and assistance from the Norwegian Public Road Administration. The work was developed as a research collaboration within the Norwegian Centre for Offshore Wind Energy, (NORCOWE, Project number: 193821 supported by the Research Council Norway) and the deployment of the lidar system was supported by Leosphere.

References

Banta, R.M., Darby, L.S., Fast, J.D., Pinto, J.O., Whiteman, C.D., Shaw, W.J., Orr, B.W., 2004. Nocturnal low-level jet in a mountain basin complex. part I: evolution and effects on local flows. J. Appl. Meteorol. 43, 1348–1365. http://dx.doi.org/10.1175/JAM2142.1.

Bingöl, F., Mann, J., Foussekis, D., 2009. Conically scanning lidar error in complex terrain. Meteorol. Z. 18, 189–195. http://dx.doi.org/10.1127/0941-2948/2009/0368.

Cheynet, E., Bogunović Jakobsen, J., Snæbjörnsson, J., 2016a. Buffeting response of a suspension bridge in complex terrain. Eng. Struct. 128, 474–487. http://dx.doi.org/10.1016/j.engstruct.2016.09.060.

Cheynet, E., Bogunović Jakobsen, J., Svardal, B., Reuder, J., Kumer, V., 2016b. Wind coherence measurement by a single pulsed Doppler wind lidar. Energy Procedia 94, 462–477. http://dx.doi.org/10.1016/j.egypro.2016.09.217.

Courtney, M., Wagner, R., Lindelöw, P., 2008. Testing and comparison of lidars for profile and turbulence measurements in wind energy. In: IOP Conference Series: Earth and Environmental Science. IOP Publishing, volume 1. doi:10.1088/1755-1315/1/1/012021.

Davenport, A.G., 1961. The application of statistical concepts to the wind loading of structures. In: ICE Proceedings, vol. 19, pp. 449. doi:10.1680/iicep.1961.11304

Drew, D.R., Barlow, J.F., Lane, S.E., 2013. Observations of wind speed profiles over Greater London, UK, using a Doppler lidar. J. Wind Eng. Ind. Aerodyn. 121, 98–105. http://dx.doi.org/10.1016/j.jweia.2013.07.019.

Fuertes, F.C., Iungo, G.V., Porté-Agel, F., 2014. 3D turbulence measurements using three synchronous wind lidars: validation against sonic anemometry. J. Atmos. Ocean. Technol. 31, 1549–1556. http://dx.doi.org/10.1175/JTECH-D-13-00206.1.

Grund, R.M., Christian, J., Banta, George, J.L., Howell, J.N., Post, M.J., Richter, R.A., Weickmann, A.M., 2001. High-resolution Doppler lidar for boundary layer and cloud research. J. Atmos. Ocean. Technol., 18, (10.1175/1520-0426(2001)018<0376:HRDLFB> 2.0.CO;2).

Hirth, B.D., Schroeder, J.L., Weiss, C.C., 2008. Surface analysis of the rear-flank downdraft outflow in two tornadic supercells. Mon. Weather Rev. 136, 2344–2363. http://dx.doi.org/10.1175/2007MWR2285.1.

Hui, M., Larsen, A., Xiang, H., 2009. Wind turbulence characteristics study at the stonecutters bridge site: part imean wind and turbulence intensities. J. Wind Eng. Ind. Aerodyn. 97, 22–36. http://dx.doi.org/10.1016/j.jweia.2008.11.002.

IEC 61400-1 (2005). IEC 61400-1 Wind turbines Part 1: Design Requirements.

Jakobsen, J.B., 1997. Span-wise structure of lift and overturning moment on a motionless bridge girder. J. Wind Eng. Ind. Aerodyn. 69, 795–805. http://dx.doi.org/10.1016/S0167-6105(97)00206-7.

Kim, D., Kim, T., Oh, G., Huh, J., Ko, K., 2016. A comparison of ground-based lidar and met mast wind measurements for wind resource assessment over various terrain conditions. J. Wind Eng. Ind. Aerodyn. 158, 109–121. http://dx.doi.org/10.1016/j.jweia.2016.09.011.

Kumer, V.-M., Reuder, J., Furevik, B.R., 2014. A comparison of lidar and radiosonde wind measurements. Energy Procedia 53, 214–220. http://dx.doi.org/10.1016/j.egypro.2014.07.230.

Lane, S., Barlow, J., Wood, C., 2013. An assessment of a three-beam Doppler lidar wind profiling method for use in urban areas. J. Wind Eng. Ind. Aerodyn. 119, 53–59. http://dx.doi.org/10.1016/j.jweia.2013.05.010.

Lange, J., Mann, J., Angelou, N., Berg, J., Sjöholm, M., Mikkelsen, T., 2015. Variations of the wake height over the Bolund escarpment measured by a scanning lidar. Bound.-Layer. Meteorol., 1–13. http://dx.doi.org/10.1007/s10546-015-0107-8.

Lenschow, D.H., Boba Stankov, B., 1986. Length Scales in the convective boundary layer. J. Atmos. Sci. 43, 1198–1209, (10.1175/1520-0469(1986)(043 < 1198:LSITCB > 2.0.CO;2).

Lhermitte, R.M., 1969. Note on the observation of small-scale atmospheric turbulence by Doppler radar techniques. Radio Sci. 4, 1241–1246. http://dx.doi.org/10.1029/RS004i012p01241.

Lothon, M., Lenschow, D., Mayor, S., 2006. Coherence and scale of vertical velocity in the convective boundary layer from a Doppler lidar. Bound.-Layer. Meteorol. 121, 521–536. http://dx.doi.org/10.1007/s10546-006-9077-1.

Lothon, M., Lenschow, D.H., Mayor, S.D., 2009. Doppler lidar measurements of vertical velocity spectra in the convective planetary boundary layer. Bound.-Layer. Meteorol. 132, 205–226. http://dx.doi.org/10.1007/s10546-009-9398-y.

Mann, J., Cariou, J.-P., Courtney, M.S., Parmentier, R., Mikkelsen, T., Wagner, R., Lindelöw, P., Sjöholm, M., Enevoldsen, K., 2009. Comparison of 3D turbulence measurements using three staring wind lidars and a sonic anemometer. Meteorol. Z. 18, 135–140. http://dx.doi.org/10.1127/0941-2948/2009/0370.

Mikkelsen, T., Mann, J., Courtney, M., Sjöholm, M., 2008. Wind Scanner: 3-D wind and turbulence measurements from three steerable Doppler lidars. In: IOP Conference Series: Earth and Environmental Science. IOP Publishing, volume 1. doi:10.1088/1755-1315/1/1/012018.

Newsom, R.K., Berg, L.K., Shaw, W.J., Fischer, M.L., 2015. Turbine-scale wind field measurements using dual-Doppler lidar. Wind Energy 18, 219–235. http://dx.doi.org/10.1002/we.1691.

Pearson, G., Davies, F., Collier, C., 2009. An analysis of the performance of the UFAM pulsed Doppler lidar for observing the boundary layer. J. Atmos. Ocean. Technol. 26, 240–250. http://dx.doi.org/10.1175/2008JTECHA1128.1.

Reitebuch, O., 2012. Wind lidar for atmospheric research. In: U.Schumann (Ed.), Atmospheric Physics Research Topics in Aerospace. Springer, Berlin, Heidelberg, pp. 487–507. doi:10.1007/978-3-642-30183-4_3.

Sathe, A., Mann, J., 2013. A review of turbulence measurements using ground-based wind lidars. Atmos. Meas. Tech. 6, 3147–3167. http://dx.doi.org/10.5194/amt-6-3147-2013.

Sathe, A., Mann, J., Gottschall, J., Courtney, M., 2011. Can wind lidars measure turbulence? J. Atmos. Ocean. Technol. 28, 853–868. http://dx.doi.org/10.1175/JTECH-D-10-05004.1.

Sathe, A., Mann, J., Vasiljevic, N., Lea, G., 2015. A six-beam method to measure turbulence statistics using ground-based wind lidars. Atmos. Meas. Tech. 8, 729–740 . http://dx.doi.org/10.5194/amt-8-729-2015.

Schneemann, J., Trabucchi, D., Trujillo, J.J., Kühn, M., 2014. Comparing measurements of the horizontal wind speed of a 2D multi-lidar and a cup anemometer. In: Journal of Physics: Conference Series. IOP Publishing, volume 555, p. 012091. doi:10.1088/1742-6596/555/1/012091.

Simley, E., Angelou, N., Mikkelsen, T., Sjöholm, M., Mann, J., Pao, L.Y., 2016. Characterization of wind velocities in the upstream induction zone of a wind turbine using scanning continuous-wave lidars. J. Renew. Sustain. Energy, 8. http://dx.doi.org/10.1063/1.4940025.

Sjöholm, M., Angelou, N., Hansen, P., Hansen, K.H., Mikkelsen, T., Haga, S., Silgjerd, J.A., Starsmore, N., 2014. Two-dimensional rotorcraft downwash flow field measurements by lidar-based wind scanners with agile beam steering. J. Atmos. Ocean. Technol. 31, 930–937. http://dx.doi.org/10.1175/JTECH-D-13-00010.1.

Sjöholm, M., Kapp, S., Kristensen, L., Mikkelsen, T., 2011. Experimental evaluation of a model for the influence of coherent wind lidars on their remote measurements of atmospheric boundary-layer turbulence. SPIE Remote Sens. Int. Soc. Opt. Photonics. http://dx.doi.org/10.1117/12.897918.

Sjöholm, M., Mikkelsen, T., Mann, J., Enevoldsen, K., Courtney, M., 2009. Spatial averaging-effects on turbulence measured by a continuous-wave coherent lidar. Meteorol. Z. 18, 281–287. http://dx.doi.org/10.1127/0941-2948/2009/0379.

Smith, D.A., Harris, M., Coffey, A.S., Mikkelsen, T., Jørgensen, H.E., Mann, J., Danielian, R., 2006. Wind lidar evaluation at the Danish wind test site in Høvsøre. Wind Energy 9, 87–93. http://dx.doi.org/10.1002/we.193.

Teunissen, H., 1980. Structure of mean winds and turbulence in the planetary boundary layer over rural terrain. Bound.-Layer. Meteorol. 19, 187–221. http://dx.doi.org/10.1007/BF00117220.

Welch, P.D., 1967. The use of fast Fourier transform for the estimation of power spectra: a method based on time averaging over short, modified periodograms. IEEE Trans. Audio Electroacoust. 5, 70–73. http://dx.doi.org/10.1109/TAU.1967.1161901.